Synchrotron X-ray Studies of Model SOFC Cathodes, Part II:

Porous Powder Cathodes

Kee-Chul Chang¹, Brian Ingram², Jan Ilavsky,³ Shiwoo Lee,^{4,5} Paul Fuoss¹ and Hoydoo You^{1*}

ABSTRACT

Infiltrated La_{0.6}Sr_{0.4}Co_{0.2}Fe_{0.8}O_{3-δ} (LSCF) sintered porous powder cathodes for solid oxide fuel cells have been investigated by synchrotron ultra-small angle x-ray scattering (USAXS). We demonstrated that atomic layer deposition (ALD) is the method for a uniform coating and liquid-phase infiltration for growing nanoscale particles on the porous LSCF surfaces. The MnO infiltrate, grown by ALD, forms a conformal layer with a uniform thickness throughout the pores evidenced by USAXS thickness fringes. The La_{0.6}Sr_{0.4}CoO₃ (LSC) and La₂Zr₂O₇ (LZO) infiltrates, grown by liquid-phase infiltration, were found to form nanoscale particles on the surfaces of LSCF particles resulting in increased surface areas. Impedance measurements suggest that the catalytic property of LSC infiltrate, not the increased surface area of LZO, is important for increasing oxygen reduction activities.

¹ Materials Science Division, Argonne National Laboratory, Argonne, IL 60439

² Chemical Sciences and Engineering Division, Argonne National Laboratory, Argonne, IL 60439

³ X-ray Science Division, Argonne National Laboratory, Argonne, IL 60439

⁴ U.S. DOE, National Energy Technology Laboratory, Morgantown, WV 26507

⁵ AECOM, Morgantown, WV 26507

^{*}hyou@anl.gov

INTRODUCTION

In solid oxide fuel cell (SOFC), mixed ionic and electronic conducting perovskite oxides such as (La,Sr)MnO_{3- δ} (LSM), (La,Sr)CoO_{3- δ} (LSC), and La_{0.6}Sr_{0.4}Co_{0.2}Fe_{0.8}O_{3- δ} (LSCF) are commonly used as cathode materials.¹ While LSM is a common cathode material for stability, significant efforts were made to search for cathode materials with a high ionic conductivity operable at lower temperatures and the cathode materials such LSC,² and its A-site variation were studied.³ More recently, LSCF⁴ is widely accepted as the cathode with a good compromise of high conductivity and stability to replace LSM.⁵ To reduce the operating temperature, the oxygen reduction reaction (ORR) activity of the porous cathodes needs to be increased as the ORR overpotential represents the most significant internal loss.^{6,7} A strategy for increasing the ORR activity is infiltrating⁸ active materials to the sintered power cathodes, which will be the focus of this paper.

Ultra-Small Angle X-ray Scattering (USAXS) is one of the best matching x-ray techniques for *in situ* study of porous powder cathodes. The pore size distributions (from nanometer to microns) of SOFC cathodes have been shown to be well matched to the USAXS capabilities. ^{9,10} More importantly, USAXS is sensitive enough to characterize the infiltrate in addition to the LSCF backbone. There are other x-ray techniques for studying the correlation of microstructure with electrochemical performance such as x-ray micro-tomography. ^{11,12} This technique can produce ~10 nm resolution real space three-dimensional images over ~10³ µm³ volume. It is non-destructive and allows imaging of the sample under operating conditions. It can also be combined with x-ray fluorescence for elemental sensitivity at the cost of worse imaging resolution. The main restriction of x-ray micro-tomography for in situ SOFC experiments is that

the sample has to be $\sim \! 10~\mu m$ thick in two dimensions, which complicates the setup of an in situ cell. Therefore, we utilize only USAXS technique for characterizing the infiltrates and LSCF backbone structures.

EXPERIMENT

Porous Sample Preparation

The main constraint in sample fabrication for USAXS is to make freestanding samples thin enough for x-ray transmission yet thick enough for sufficient scattering intensity. For x-ray energy above 16 keV the samples were made by a screen printing technique. Approximately 10 µm thick layers of cathodes and YSZ, schematically shown in Figure 1, was printed on 0.3 mm thick Al₂O₃(0001) or 0.5mm thick MgO(001) single crystal substrate. The screen printed LSCF was annealed at 1000°C for ~1 hour to burn out the polymers in the ink and to sinter the powders. YSZ was annealed at 1400°C for use as an electrolyte in SOFC cell or 1200°C just as a backbone structure of infiltrates, respectively. Because of the well-known solubility of YSZ and Al₂O₃ above ~1400°C, some critical experiments were repeated with MgO substrates to ensure the results presented here are not affected by the formation of the solid solution. Even though the infiltrated cathodes are the main purpose, USAXS measurements from three different types of samples are used to investigate systematically: (i) LSCF on Al₂O₃ substrates to determine the

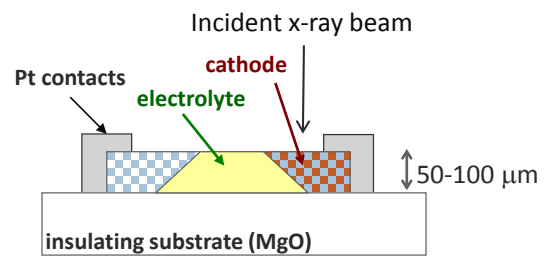


Figure 1. Schematic illustrations of the experimental setups for porous cathodes in a symmetric cell configuration operated in a half-cell configuration for a transmission geometry

ideal thickness for USAXS, (ii) a symmetric SOFC cell test structure on MgO, (iii) a LSCF infiltrated YSZ on MgO for *in situ* temperature processing measurements. The final samples were the LSCF porous powders infiltrated by MnO, using an atomic layer deposition (ALD) technique, and LSC and LaZrO₃ (LZO), using a liquid-phase infiltration technique.

USAXS Measurement

The small angle x-ray scattering (SAXS) technique ^{13,14} probes the average particle size, particle size distribution, and the surface-to-volume ratio at length scales of 1 to 100 nm. The length scale can be extended to ~1 μm in Ultra Small Angle X-ray Scattering (USAXS)¹⁵ technique. We used the USAXS instrument at sector 15 (ChemMat CARS) at APS.¹⁶ The instrument uses Bonse-Hart¹⁷ double-crystal configuration for scattering vector ranges of ~10⁻⁴ to ~10 Å⁻¹, which are equivalent to the length sensitivity to ~10 μm to ~10 nm length scale. The double-crystal configuration uses a pair of multiple-bounce channel cut monochromator and analyzer, in order to increase the resolution and discriminate the diffraction from the intense main beam. It uses an undulator source for a dynamic intensity range of 10⁸ to 10⁹ depending on the configuration. We used 16~18 keV for our experiments. Linkam TS1500 heater, ¹⁸ equipped with sapphire windows and capable of heating to 1500°C, was used for *in situ* heating experiments. The resulting USAXS data was analyzed using Irena small angle scattering analysis software suite. ¹⁹

RESULTS AND DISCUSSION

Porod's Law and Thickness Fringes

Ultra-small angle x-ray scattering can be used to examine the distribution of an average particle and pore sizes ranging from ~10 nm to ~10 µm. In analyzing and understanding the x-ray reflectivity or small-angle scattering, it is convenient to write an equation for the scattering intensity from interfaces. Here we define an interface to be an elemental area whose electron density changes only in the normal direction. We call 'x-ray reflectivity' when the interfaces form an overall relatively well-defined flat surface and 'small-angle scattering' when the interfaces are complex and often convoluted. In both cases, x-rays scatter only from the interfaces. The interface scattering can be then written in two terms:²⁰

$$I(q) = \sum_{n=1}^{N} V_n^2(q) + 2 \sum_{m < n}^{N} V_m(q) \cdot V_n(q) \cos(\varphi_m - \varphi_n)$$
 (1)

where $V_n(q)$ is a reflection amplitude from n^{th} interface, $\varphi_m - \varphi_n = qd$ is the phase difference associated with the distance between the layers. The first term represents the sum of scattering intensities from individual interfaces and the second term represents the interference between them. This derivation is essentially a Hendricks and Teller expansion²¹ approach for the better known Ciccariello and Benedetti's oscillatory deviations, ²², ²³ which can be obtained by angular average of Eq. (1).

The amplitude $V \approx \left(\frac{q_c}{2q}\right)^2$ with q_c being the critical angle of the interface that is proportional to the electron-density jump at the interface. This is a good approximation for USAXS from complex interfaces where the scattering can be approximated to a kinematic limit.

The first term then behaves smoothly with a function q^{-4} following Porod's law. The second term behaves similarly except for the oscillatory term multiplied. For random layer thicknesses, the oscillatory terms are averaged and cancelled out. Then the overall scattering, the first term plus the second term, recovers the Porod's law. However, for a conformal roughness, where the thickness of the overlayer is uniform, the unique thickness fringe of the cosine term can ride on the Porod's law behavior.

MnO Infiltrate Grown by Atomic Layer Deposition on LSCF

Infiltration techniques have been successful in improving catalytic activities.⁸ While the liquid-phase infiltration has been successful, e.g., LSM infiltration to LSCF cathodes,²⁴ in improving the stability and catalytic activity, we explored a gas-phase infiltration, Atomic Layer Deposition (ALD) technique, for better penetration of the infiltrates deep into the porous cathode materials. As the first step, we tested the ALD of MnO on LSCF thin film, epitaxially grown on NdGaO₃ (011) substrate by pulse laser deposition (PLD).²⁵ The film was examined with x-ray reflectivity (XR) technique before the ALD, after the ALD, and after annealing the ALD layer.

The thickness of LSCF films was ~10 nm thick pre-determined by a XR measurement and that of MnO was nominally ~5 nm. Figure 2(a) shows the evolution of the XR on this sample annealed to 700°C. The XR at room temperature (RT) shows a fringe of ~0.05 Å⁻¹. This corresponds to the overall thickness of ~15 nm as expected. Annealing it to 500°C makes the XR change significantly. However, there is not much change in the average fringe width, therefore, the overall thickness. Analysis of the data indicates that the major change occurs on the surface roughness. The XR decreases at large $Q > 0.3 \text{ Å}^{-1}$ by annealing at 500°C. This occurs because

the roughness of the MnO/LSCF interface increases from 2 to 5 Å. The roughness of MnO surface, which was initially measured at ~10 Å at RT, appears decreasing to ~5 Å by annealing at 500°C. This can happen when the MnO layer is partially conformal to the MnO/LSCF interface. The total roughness remains ~10 Å as before because the roughness of the underlying MnO/LSCF layer is already at 5 Å. This result suggests that the initially grown ALD layer undergoes conformal layering at 500C, i.e., forming a rather uniform MnO layer following the undulation of LSCF surface.

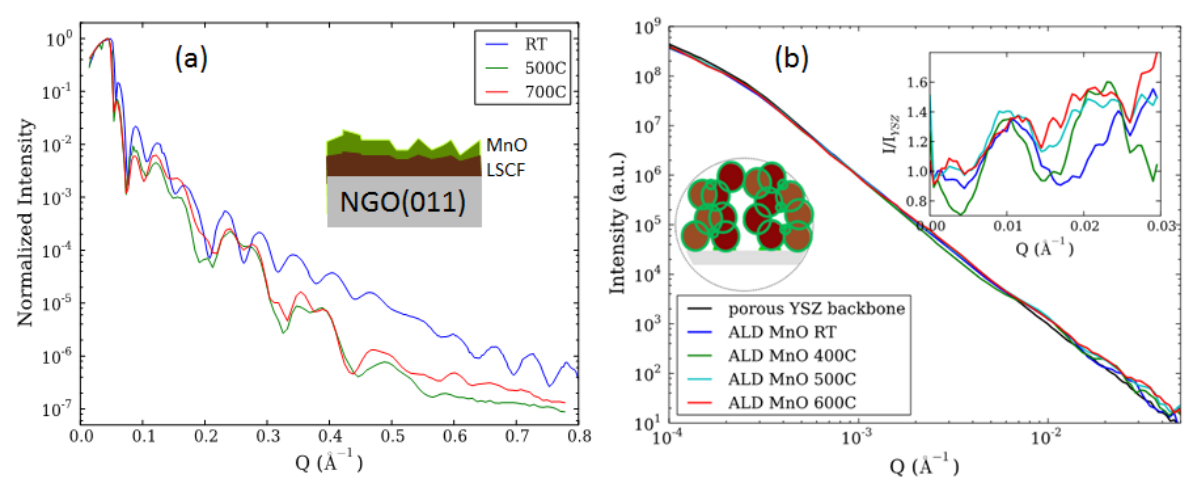


Figure 2. (a) X-ray reflectivity of ~5 nm thick MnO on ~10 nm LSCF epitaxially grown on a NGO(011) substrate. The inset illustrates the partial conformal roughening of the MnO+LSCF layers. (b) *Ex-situ* USAXS data from the 50 nm ALD MnO infiltrate grown on porous YSZ backbone at different temperatures. The inset shows the ratio of the USAXS intensity to that of the YSZ backbone.

With the evidence of the conformal ALD growth on the film cathodes, we tested the feasibility with the porous samples: ALD deposition of MnO on sintered porous YSZ backbone. We prepared samples with nominally 10 and 50 nm thick MnO layers. However, the preliminary USAXS pattern from the 10 nm thick sample was almost indistinguishable from that obtained from the YSZ backbone. Therefore, we focus on the 50 nm thick MnO infiltrate layer annealed at from RT to 800°C. The *ex situ* USAXS data taken at several temperatures are compared to that

of the backbone in Figure 2(b). The ALD layer results in the fringes at high Q values of USAXS data. The fringes can be seen more clearly by dividing the data by the backbone data and they are shown in the inset of Figure 2(b).

Using the oscillatory term of Eq. (1), $\cos(2\pi Qd)$ with $q=2\pi Q$, we can estimate the thickness of MnO infiltrate. Since the ALD process and the annealing to 600° C are not expected to increase YSZ particle sizes significantly, we can estimate the average MnO layer thickness from the fringe period. Although noisy, the first maximum in the fringes is at $\Delta Q=0.01$ Å⁻¹, and we can estimate that the ALD film thickness is ~60 nm using $d=2\pi/\Delta Q$. The fringes grow less distinct at 600° C suggesting that the ALD film may start to lose uniformity at this temperature. This suggests that USAXS is an effective technique for the morphological characterizations after infiltration by gas phase ALD. However, multi-component ALD of La, Sr, and Mn oxides, which is required to complete the porous cathodes by the ALD technique, was beyond the scope of our study and expertise and has not been pursued. Our feasibility study simply demonstrates that the ALD technique is a potential alternative growth technique for porous cathodes and USAX is the characterization technique for ALD growth studies.

Liquid-phase infiltration of LSC and LZO on LSCF

We performed liquid-phase infiltration of LSCF, LSCF+LSC, and LSCF+LZO on YSZ backbones. The evolution of the microstructures during infiltration and subsequent annealing process was tracked with USAXS in temperature and time (Figure 3). First, the screen-printed porous YSZ backbone was infiltrated with LSCF in tartaric acid. Note that there is a large difference in the overall intensity between the RT data and the data at 400°C and higher

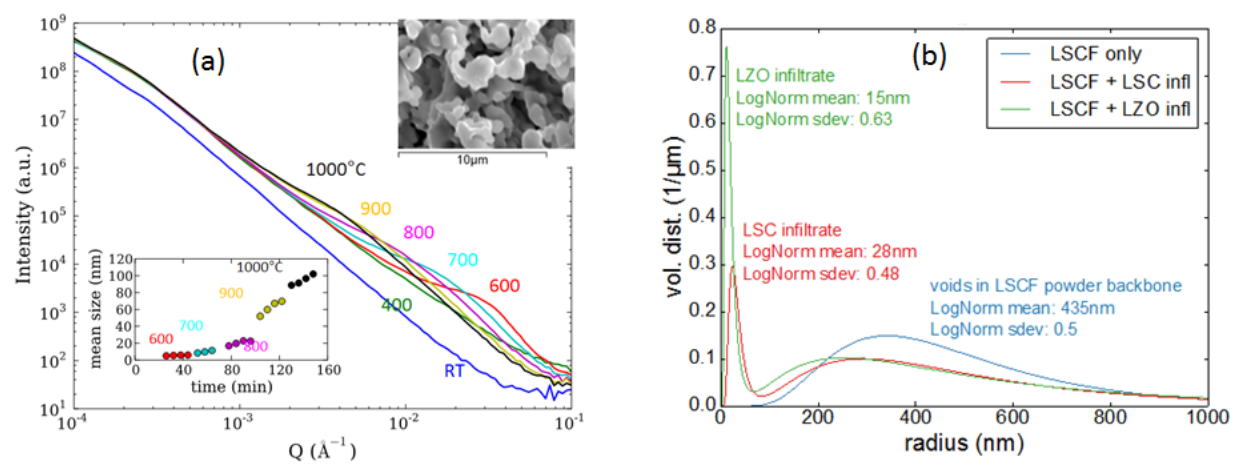


Figure 3. (a) In situ USAXS of tartaric acid based LSCF grown on porous YSZ during annealing to 1000°C. (b) The fitted log-normal volume distribution profile of the scatters in the USAXS data.

temperatures. At RT, the presence of the organics reduces the interfacial density difference and, therefore, the scattering power, V_n , in Eq. (1).

From 400°C to 1000°C, there is no change in the overall intensity. Instead, a peak-like feature appears and moves to smaller Q as the temperature increases. The peak appears because infiltrates begin to nucleate and it moves to smaller Q values because the size of the infiltrates grows. A rough estimation of the particle size can be made from the widths of the peaks, although the results of careful fits will be discussed later. Based on the estimation, the infiltrates begin to nucleate to ~1 nm at 600°C and continue to coarsen slowly to ~5 nm at 700°C. Then, coarsening accelerates and the particle size becomes over 100 nm at ~1000°C.

Three identical LSCF samples were made with the infiltration to the YSZ backbones. The samples were then annealed for an hour at 1000°C. Then two were subsequently infiltrated with La_{0.6}Sr_{0.4}CoO₃ (LSC) and La₂Zr₂O₇ (LZO) and calcined at 850°C. These infiltrates were chosen to delineate the influence of infiltrate properties from infiltrate induced microstructure on electrochemical performance. LSC is chosen for the known high catalytic activity and LZO is chosen for catalytically neutral due to its relatively low conductivity.

The all three samples were then characterized using USAXS and XRD. Fitting the USAXS data sets from the three samples, the size distributions of the LSCF powder and infiltrates were obtained, assuming spherical particles and log-normal volume distribution. The log-normal distributions are shown in Figure 3(b). They reveal that the LSC and LZO infiltrates are 56 nm and 30 nm in diameter, respectively. From the size distributions, we also obtained that the surface areas of LSC and LZO infiltrates are ~2 and ~6 times the surface area of the LSCF powder only. Both infiltrates increase the surface area. But LZO increases significantly more than LSC.

High-resolution XRD measurements were obtained using an area detector. Use of the area detector not only improves the overall measured intensity but also increase the resolution by integrating the data pixel by pixel. The high-resolution patterns help to confirm the phases of the infiltrates. The resulting XRD scans are shown in Figure 4. It is easy to index the strong peaks

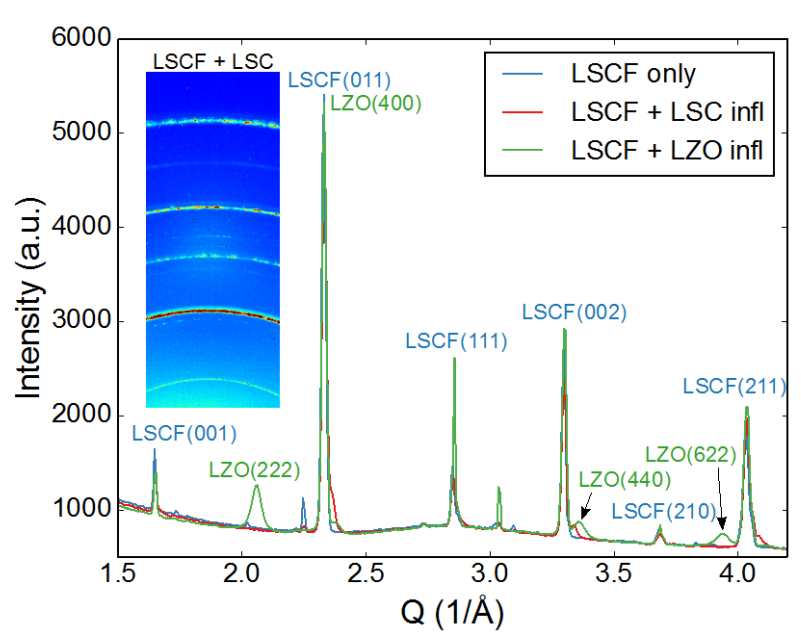


Figure 4. XRD of LSCF powder and LSCF powder infiltrated with LSC or LZO. The high-resolution patterns are obtained from images of the area detector shown in the inset. The XRD verifies the presence of LSC and LZO phases in the sample.

from the perovskite LSCF powder. It is also simple to index the significantly weaker peaks for the pyrochlore structure of LZO infiltrates. However, it is difficult to index the LSC peaks because LSC has a similar structure with LSCF and their peaks nearly overlap each other. However, in a close examination, the peaks from LSC can be distinguished as small high-angle shoulders to the main LSCF peak. These XRD patterns verify the phases of the infiltrates.

After the verification of the phases, we took impedance measurements on these samples at 750°C as shown in Figure 4. The spectra were fitted with an equivalent circuit composed of a serial resistance (Rs), a polarization resistance (Rp), and a constant phase element (CPE) in parallel as shown in the inset. The values of Rp calculated from the equivalent circuit fitting were 431 k Ω , 324 k Ω , and 253 k Ω for LSCF baseline, LZO-infiltrated LSCF, and LSCo-infiltrated LSCF, respectively. The smaller polarization resistance of the LSC infiltrated sample compared with that of the LSCF powder suggests that the surface-modifying LSC is effective in

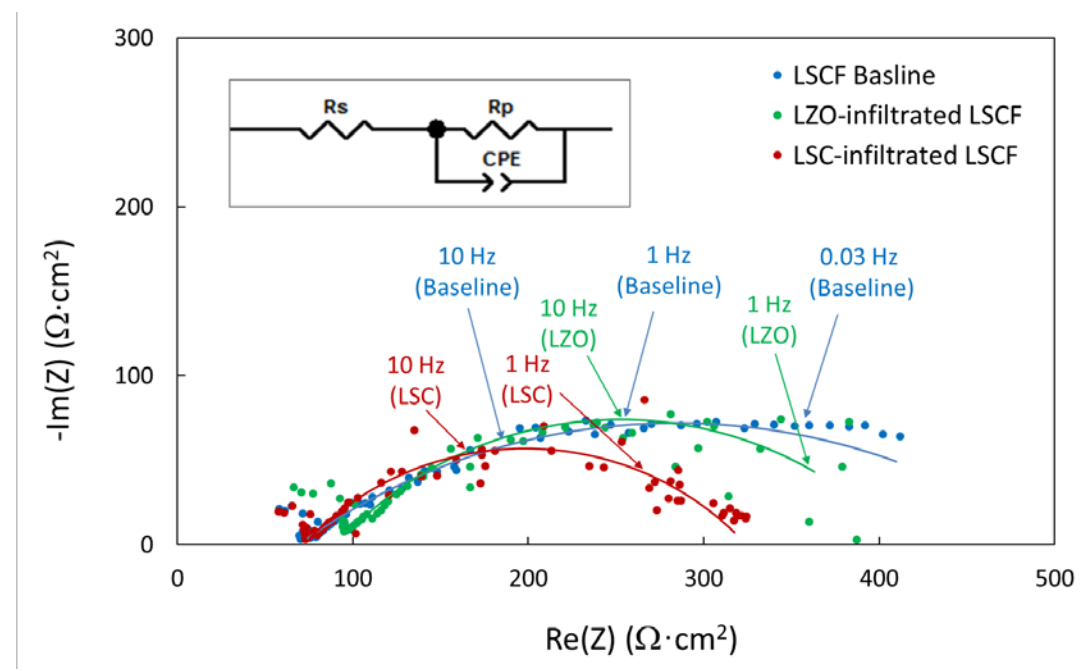


Figure 5: Nyquist plot of the USAXS samples at 750°C after x-ray characterization. Solid lines are simulated data fitted with the equivalent circuit model presented in the inset.

activating LSCF cathode. Although the LZO infiltrates are smaller in size and have larger total surface area compared to the LSC, the polarization resistance of LZO-infiltrated LSCF is higher than that of LSC-infiltrated LSCF, indicating that conductivity and catalytic activity dominantly affect performance of the infiltrated electrodes. The highest Rp of the LSCF baseline is attributable to the abnormal concentration polarization indicated by the extra arc at the frequency range below 1 Hz²⁷. The origin of the gas diffusion limitation indicated by the baseline is unclear, but it may not be related with catalytic activity of cathode. Rather, the impedance arc associated with ORR activity of cathode is generally apparent at the intermediate frequency range (~10 Hz). It is noticeable that LZO-infiltrated cathode has higher resistance near 10 Hz than the baseline cathode, which shows that electrically insulating LZO infiltrate deactivate LSCF cathode.

SUMMARY

We demonstrated the effectiveness of USAXS measurements for the characterization of powder electrodes. The technique is particularly powerful in studying infiltrated powder samples, in which the size distribution of the infiltrates is much smaller than that of the pores in the powder. Using USAXS, we can study formation and the size evolution of infiltrates under realistic cell operation conditions. We presented examples for the Ciccariello and Benedetti's oscillatory deviations in the USAXS measurements; cathode layer formation on porous electrolytes and conformal deposition of infiltrates on cathode materials. The non-destructive x-ray characterizations of symmetric cells with infiltrated electrodes enabled us to quantify the size distribution, total volume, and the phase of the infiltrates. Electrochemical testing showed that

the improved performance of LSC infiltrated sample is well beyond the simple geometric effect, such as increases in surface area and triple phase boundary due to the infiltration, in agreement with the previous studies.²⁶

ACKNOWLEDGMENTS

The work by PF and HY was supported by the U.S. Department of Energy (DOE), Office of Science, Office of Basic Energy Sciences (BES), Division of Materials Science and Engineering, the work by KC and BI was supported by Solid State Energy Conversion Alliance (SECA). ChemMatCARS Sector 15 is principally supported by the Divisions of Chemistry (CHE) and Materials Research (DMR), National Science Foundation, under grant number NSF/CHE-1346572. Use of the Advanced Photon Source, an Office of Science User Facility operated for the U.S. Department of Energy (DOE) Office of Science by Argonne National Laboratory, was supported by the U.S. DOE under Contract No. DE-AC02-06CH11357.

REFERENCES

- ¹ S. B. Adler, Chem. Rev., 104, 4791 (2004).
- ² A. N. Petrov, O. F. Kononchuk, A. V. Andreev, V. A. Cherepanov, and P. Kofstad,, Solid State Ionics, 80, 189 (1995).
- ³ J. M. Ralph, A. C. Schoeler, and M. Krumpelt, J. Mater. Sci., 36, 1161 (2001).
- ⁴ L.-W. Tai, M.M. Nasrallah, H.U. Anderson, D.M. Sparlin, and S.R. Sehlin, Solid State lonics 76, 261 (1995); ibid, 76, 273 (1995).
- ⁵ S.P. Jiang, Solid State Ionics, 146, 1 (2002).
- ⁶ C. Xia and M. Liu, Adv Mater 14, 521 (2002).
- ⁷ Y. Choi, D.S. Mebane, J. Wang, M. Liu, Top Catal, 46, 386 (2007).
- ⁸ D. Ding, X. Li, S.Y. Lai, K. Gerdes, and M. Liu, Energy & Environmental Science, 7, 552 (2014).
- ⁹ A. J. Allen, J. Am. Ceram. Soc., 88, 1367 (2005).
- ¹⁰ A. J. Allen, J. Ilavsky, and A. Braun, Adv. Eng. Mater., 11, 495 (2009).
- ¹¹ P. R. Shearing et al., Electrochem. Solid-State Lett., 14, B117 (2011).
- ¹² K. N. Grew et al., J. Electrochem. Soc., 157, B783 (2010).
- ¹³ R.-J. Roe, Methods of X-ray and neutron scattering in polymer science, Oxford University Press, 2000.
- ¹⁴ O. Glatter, O. Kratky, eds., Small angle x-ray scattering, Academic Press, 1982.
- ¹⁵ J. Ilavsky, P.R. Jemian, A.J. Allen, F. Zhang, L.E. Levine, G.G. Long, J. Appl. Crystallogr., 42, 469 (2009).
- ¹⁶ J. Ilavsky et al., *Journal of Applied Crystallography*, **42**, 469–479 (2009).

- ¹⁷ U. Bonse and M. Hart, Appl. Phys. Lett., 6, 155 (1965).
- ¹⁸ Linkam Scientific, Tadworth, UK (www.linkam.co.uk).
- ¹⁹ J. Ilavsky and P. R. Jemian, *J. Appl. Cryst.*, **42**, 347 (2009).
- ²⁰ H. You, C. Melendres, Z. Nagy, V.A. Maroni, W. Yun, R.M. Yonco, Phys. Rev. B 45 11288 (1992).
- ²¹ S. Hendricks and E. Teller, J. Chem. Phys. 10, 147 (1942).
- ²² S. Ciccariello and A. Benedetti, J. Appl. Cryst. 19, 195 (1986).
- ²³ A. Benedetti and S. Ciccariello, J. Appl. Cryst. 27, 249 (1994).
- ²⁴ X. Lou, Z. Liu, S. Wang, Y. Xiu, C.P. Wong, M. Liu, J. Power Sources, 195 419 (2010).
- ²⁵ The previous paper: K.-C. Chang, B. Ingram, J. Ilavsky, S. Lee, P. Fuoss, and H. You, submitted.
- ²⁶ S. Lee, N. Miller, H. Abernathy, K. Gerdes, A. Manivannan, J. Electrochem. Soc., Vol 158, pp B735 (2011).
- ²⁷ C. Endler, A. Leonide, A. Weber, F. Tietz, and E. Ivers-Tiffee, J. Electrochem. Soc., 157, B292 (2010).